

First principles study of the vibronic coupling in positively charged C_{60}^+

Zhishuo Huang^{1, a)} and Dan Liu^{2, 1, b)}

¹⁾*Theory of Nanomaterials Group, KU Leuven, Celestijnenlaan 200F, B-3001 Leuven, Belgium*

²⁾*Institute of Flexible Electronics (IFE), Northwestern Polytechnical University, 127 West Youyi Road, Xian, 710072, Shaanxi, China*

(Dated: 13 March 2020)

Vibronic coupling parameters for C_{60}^+ were derived via DFT calculations with hybrid B3LYP and CAM-B3LYP functional, based on which the static Jahn-Teller effect were analyzed. The global minima of adiabatic potential energy surface (APES) shows a D_{5d} Jahn-Teller deformation, with stabilization energies of 110 and 129 meV (with B3LYP and CAM-B3LYP respectively), which are two times larger than that in C_{60}^- , suggesting the crucial role of the dynamical Jahn-Teller effect. Present results enable us to assess the actual situation of dynamical Jahn-Teller effect in C_{60}^+ and excited C_{60} in combination with the established parameters for C_{60}^- .

I. INTRODUCTION

Recent experimental confirmation of the presence of C_{60}^+ as interstellar materials^{1,2} renewed the interests in C_{60} cations, and burst various spectroscopic and theoretical investigations on C_{60}^+ and related systems³⁻⁸. It is known that C_{60} in its charged and excited states exhibits complex Jahn-Teller (JT) effect due to its high symmetry (I_h)^{9,10}. In particular, JT effect in C_{60}^+ is one of the most involved cases because of the five-fold degenerate highest occupied molecular orbitals (HOMOs) of C_{60} . Toward understanding JT effect in C_{60}^{n+} cations, spectroscopic¹¹⁻¹³ and theoretical¹⁴⁻²² investigations have been piled up.

Realistic description of JT effect in positively charged C_{60} relies on the combination of an adequate model and accurate enough vibronic coupling parameters. Derivations of vibronic coupling parameters have been addressed²³⁻²⁵, and comprehensive sets of parameters have been estimated by density functional theory (DFT) calculations at local density approximation (LDA) level^{23,25}. Nevertheless, in studies about C_{60}^- , it has been shown that LDA tends to underestimate the coupling parameters²⁶, while hybrid B3LYP functional is found to give closer parameters to the experimental data. Furthermore, a good agreement between B3LYP and GW approximation calculations²⁷ supports the accuracy of hybrid functional in studies of C_{60} . Besides, one recent study showed that B3LYP with long-range interaction correction, CAM-B3LYP, could improve the accuracy of vibronic parameters in C_{60}^- with respect to experimental data, indicating CAM-B3LYP could give vibronic parameters much closer to the real situation²⁸. Therefore, it is desired to derive the coupling parameters at a better level than LDA for accurate description of C_{60} cations.

In this work, we derived orbital vibronic coupling parameters for C_{60}^+ via DFT calculations with both B3LYP

and CAM-B3LYP hybrid functionals. These obtained vibronic coupling parameters were compared with the previous data obtained by LDA calculations. Based on these parameters, the adiabatic potential energy surface (APES) was analyzed, and the symmetry of JT deformed C_{60}^+ as well as static JT energies were established.

II. VIBRONIC HAMILTONIAN

The highest occupied molecular orbitals (HOMOs) of C_{60} with I_h symmetry²⁹ are characterized by five-fold degenerate h_u irreducible representation. According to selection rule, these orbitals linearly couple to mass-weighted normal vibrational modes involved in the symmetric product of h_u representation³⁰:

$$[h_u \otimes h_u] = a_g \oplus g_g \oplus 2h_g. \quad (1)$$

Among them, g_g and h_g modes are JT active, while a_g is not because it does not change the symmetry of molecules. Thus, taking the equilibrium structure of neutral C_{60} as the reference, $H \otimes (a \oplus g \oplus 2h)$ JT Hamiltonian for C_{60}^+ is expressed as^{9,10,14}

$$\begin{aligned} H &= H_0 + H_{JT}, \quad (2) \\ H_0 &= \frac{1}{2} (p_a^2 + \omega_a^2 q_a^2) + V_a q_a + \sum_{\gamma=a,x,y,z} \frac{1}{2} (p_{g\gamma}^2 + \omega_g^2 q_{g\gamma}^2) \\ &\quad + \sum_{\gamma=\theta,\epsilon,\xi,\eta,\zeta} \frac{1}{2} (p_{h\gamma}^2 + \omega_h^2 q_{h\gamma}^2), \quad (3) \\ H_{JT} &= V_g \sum_{\gamma=a,x,y,z} \hat{C}_{g\gamma} q_{g\gamma} + \frac{\sqrt{5}V_{1h}}{2} \sum_{\gamma=\theta,\epsilon,\xi,\eta,\zeta} \hat{C}_{1h\gamma} q_{1h\gamma} \\ &\quad + \frac{\sqrt{5}V_{2h}}{2} \sum_{\gamma=\theta,\epsilon,\xi,\eta,\zeta} \hat{C}_{2h\gamma} q_{2h\gamma} \quad (4) \end{aligned}$$

where ω_Γ ($\Gamma = a_g, g_g, h_g$) are vibration frequencies, q_Γ are mass-weighted normal coordinates³¹, V_Γ is vibronic coupling parameter for Γ mode, and $\hat{C}_{\Gamma\gamma}$ ($\gamma = a, x, y, z, \theta, \epsilon, \xi, \eta, \zeta$) are the Clebsch-Gordan coefficients, which are taken from Ref.³² and listed in Appendix A. A coefficient $\sqrt{5}/2$ is multiplied to vibronic couplings terms of

^{a)}Electronic mail: zhishuohuang@gmail.com

^{b)}Electronic mail: iamdliu@nwpu.edu.cn

h_g modes so that JT energy becomes:

$$E_g^{\text{JT}} = -\frac{V_g^2}{2\omega_g^2}, \quad E_{nh}^{\text{JT}} = -\frac{V_{nh}^2}{2\omega_h^2}, \quad (n = 1, 2). \quad (5)$$

There are two vibronic couplings to one h_g mode because h_g representation appears twice in selection rule, Eq. (1). The basis of vibronic Hamiltonian matrices are H_u electronic states of C_{60}^+ in the order of $|H_u\theta\rangle$, $|H_u\epsilon\rangle$, $|H_u\xi\rangle$, $|H_u\eta\rangle$, $|H_u\zeta\rangle$. For h_g and h_u representations, d orbital type basis are used, and hence, $\theta, \epsilon, \xi, \eta, \zeta$ transform as $(2z^2 - x^2 - y^2)/\sqrt{6}$, $(x^2 - y^2)/\sqrt{2}$, $\sqrt{2}yz$, $\sqrt{2}zx$, $\sqrt{2}xy$, respectively, under rotation. Although C_{60} has two a_g , six and eight sets of g_g and h_g modes, respectively, and indices distinguishing them are not explicitly written in Eq. (3) for simplicity. Phase factors of mass-weighted normal modes are the same as those in the Supplemental Materials of Ref.³². Since the equilibrium geometry of C_{60} is chosen as the reference structure of C_{60}^+ , vibronic coupling parameters of totally symmetric modes are also nonzero. JT energy by totally symmetric deformation is

$$E_a = -\frac{V_a^2}{2\omega_a^2}. \quad (6)$$

In many other literatures, like the work of A. Ceulemans¹⁴, linear combinations of real d -type functions, d_{z^2} , $d_{x^2-y^2}$, are used, which could be transformed into irreducible representation in this work by

$$q_\theta = \sqrt{\frac{5}{8}}Q_\theta + \sqrt{\frac{3}{8}}Q_\epsilon, \quad q_\epsilon = \sqrt{\frac{3}{8}}Q_\theta - \sqrt{\frac{5}{8}}Q_\epsilon, \quad (7)$$

where Q_θ and Q_ϵ are normal coordinates in Ref.¹⁴, while q_θ and q_ϵ are normal coordinates in this work, resulting in the relation between coupling parameters V_{1h} and V_{2h} in this work and F_{Hb} and F_{Ha} defined in Ref. 14:

$$V_{1h} = \frac{F_{Hb}}{4\sqrt{5}}, \quad V_{2h} = \frac{F_{Ha}}{12\sqrt{5}}. \quad (8)$$

The modification introduced here is to treat the JT Hamiltonian in a framework consistent to the standard one in C_{60}^- ⁹.

III. RESULTS

A. Orbital vibronic coupling parameters

Vibronic coupling constants of C_{60} have been most intensively investigated in the case of C_{60}^- , and coupling constants have been derived by various methods. By definition, vibronic coupling parameters for JT active h_g modes, $V_{h_g}^-$, can be derived by²⁶

$$V_{h_g}^- = -\left. \frac{\partial E_z^-(\mathbf{q}_{h_g})}{\partial q_{h_g\theta}} \right|_{\mathbf{q}_{h_g}=\mathbf{0}}, \quad (9)$$

where $E_z^-(\mathbf{q}_{h_g}) = \langle T_{1uz} | \hat{H}^- | T_{1uz} \rangle$, $|T_{1uz}\rangle$ is t_{1uz} electronic state of C_{60}^- , \hat{H}^- is Hamiltonian for C_{60}^- , and $\mathbf{q}_{h_g} = \mathbf{0}$ indicates equilibrium structure of C_{60} . Because of symmetry, contributions from occupied orbitals are zero, and only partially filled t_{1u} orbital level contribute to vibronic couplings. In the case of C_{60}^- , the nature of t_{1u} orbitals do not differ from that of neutral C_{60} : although t_{1u} orbitals are mixed with the other t_{1u} orbitals, the mixing is very small due to high symmetry, and orbitals are separated from each other by large orbital energy gaps. Consequently, gradients of total energy can be approximated by those of orbital energy levels with respect to normal modes of neutral C_{60} . Indeed, in the case of C_{60}^- , these two approaches give very close results^{26,27,32,33}.

Similar situation is expected in C_{60}^+ : the nature of the h_u orbital does not change by adding one hole to the same molecular structure. Thus, orbital vibronic coupling parameters of neutral C_{60} can be used to express vibronic coupling parameters of C_{60}^+ . Since C_{60}^+ has one hole in h_u HOMOs, it is convenient to perform particle-hole transformation³⁴, under which, the sign of orbital vibronic coupling parameter for one electron in HOMOs of C_{60} should be inverted for that in the case of one hole in HOMOs. Therefore,

$$V_\Gamma = -v_\Gamma, \quad (10)$$

where v_Γ is one orbital vibronic coupling parameter for C_{60} and V_Γ is the parameter for C_{60}^+ .

Orbital vibronic coupling parameters were calculated using frozen-phonon approach. Orbital energy levels of distorted C_{60} are fitted to the eigenvalues of JT Hamiltonian matrix (Eq. (4)). In the present case, $h_g(\mu)\epsilon$ and $g_g(\mu)a$ deformations are used because diagonalizing the model Hamiltonian is easier. For DFT calculations, a triple-zeta basis set [6-311G(d)] was employed for both B3LYP and CAM-B3LYP functionals within Gaussian³⁵. Some fittings are shown in Fig. 1 (see Supplemental Materials for other fittings). Black points indicate DFT levels originating from HOMOs, with gray lines for energy level calculated from model Hamiltonian. Derived orbital vibronic coupling parameters are shown in Table I. From this table, JT stabilization energies for different JT active modes are improved about 30 % with CAM-B3LYP compared with these with B3LYP. One should note that there is almost no nonlinear splitting due to vibronic effect in HOMO levels, indicating weak quadratic or higher vibronic couplings as in the case of C_{60}^- ³². This guarantees the validity of linear vibronic model (Eq. (3)) for the description of JT effect of C_{60} cations.

B. Static Jahn-Teller effect

Vibronic coupling lifts degeneracy with the deformation keeping one of the highest subgroup symmetries³⁶, resulting in six D_{5d} and ten D_{3d} minima¹⁴, as there are six C_5 and ten C_3 axes in C_{60} . Thus, based on present

TABLE I. The frequencies ω_Γ (cm^{-1}), orbital vibronic coupling parameters v_Γ (10^{-4} a.u.), and stabilization energies E_Γ (meV) for the a_g , g_g , and h_g modes. The data calculated with B3LYP for LUMOs are taken from Ref.³². $g_\Gamma = V_\Gamma/\sqrt{\hbar\omega_\Gamma^3}$ is dimensionless vibronic coupling parameter.

μ	ω_Γ	B3LYP				CAM-B3LYP									
		v_Γ		g_Γ		E_Γ		ω_Γ		v_Γ		g_Γ		E_Γ	
		1	2	1	2	1	2	1	2	1	2	1	2	1	2
HOMO															
a_{g1}	497	-0.121		-0.112		0.389		506		-0.118		-0.106		0.355	
a_{g2}	1498	1.040		0.184		3.159		1527		1.369		0.236		5.268	
g_{g1}	481	-0.375		-0.366		3.984		502		-0.405		-0.370		4.265	
g_{g2}	584	-0.101		-0.074		0.196		586		-0.207		-0.150		0.815	
g_{g3}	768	0.923		0.446		9.466		787		1.083		0.504		12.400	
g_{g4}	1092	-1.281		-0.365		9.019		1092		-1.583		-0.451		13.781	
g_{g5}	1335	0.541		0.114		1.076		1356		0.739		0.152		1.947	
g_{g6}	1540	1.477		0.251		6.029		1576		1.571		0.258		6.509	
h_{g1}	266	0.690	-0.080	1.635	-0.190	44.099	0.593	271	0.727	-0.090	1.674	-0.206	47.120	0.714	
h_{g2}	439	-0.508	-0.290	-0.568	-0.324	8.776	2.860	450	-0.558	-0.363	-0.601	-0.391	10.063	4.269	
h_{g3}	726	-0.043	0.977	-0.023	0.514	0.023	11.869	745	-0.061	1.053	-0.031	0.532	0.043	13.086	
h_{g4}	786	0.923	-0.059	0.431	-0.027	9.038	0.037	802	0.930	-0.139	0.421	-0.063	8.821	0.198	
h_{g5}	1125	-0.101	-0.495	-0.028	-0.135	0.053	1.269	1148	-0.074	-0.565	-0.020	-0.150	0.028	1.591	
h_{g6}	1269	0.965	0.272	0.220	0.062	3.790	0.301	1300	0.986	0.025	0.216	0.005	3.768	0.002	
h_{g7}	1443	2.860	1.487	0.537	0.279	25.745	6.960	1480	3.425	2.010	0.618	0.363	35.072	12.081	
h_{g8}	1607	2.721	-1.542	0.434	-0.246	18.790	6.034	1663	3.217	-1.701	0.488	-0.258	24.523	6.854	
LUMO															
a_{g1}	497	-0.264		-0.245		1.849		506		-0.253		-0.228		1.629	
a_{g2}	1498	-2.380		-0.422		16.543		1527		-2.921		-0.503		23.971	
h_{g1}	266	0.192		0.455		3.415		271		0.209		0.481		3.884	
h_{g2}	439	0.450		0.503		6.886		450		0.456		0.491		6.735	
h_{g3}	726	0.754		0.396		7.069		745		0.849		0.429		8.512	
h_{g4}	786	0.554		0.259		3.256		802		0.575		0.260		3.367	
h_{g5}	1125	0.766		0.209		3.038		1148		0.827		0.219		3.402	
h_{g6}	1269	0.578		0.132		1.360		1300		0.513		0.113		1.019	
h_{g7}	1443	2.099		0.394		13.867		1480		2.553		0.461		19.492	
h_{g8}	1607	2.043		0.326		10.592		1663		2.325		0.352		12.808	

basis, using symmetry adapted deformations²⁰, deformations for D_{5d} and D_{3d} minima are expressed by

$$\begin{aligned} \mathbf{q}_{h_g}^{D_{5d}} &= q_{h_g} \left(\frac{\phi^2}{2\sqrt{5}}, \frac{\phi^{-1}}{2} \sqrt{\frac{3}{5}}, 0, \sqrt{\frac{3}{5}}, 0 \right), \\ \mathbf{q}_{g_g}^{D_{5d}} &= q_{g_g} (0, 0, 0, 0), \end{aligned} \quad (11)$$

and

$$\mathbf{q}_{h_g}^{D_{3d}} = q_{h_g} \left(-\frac{\phi^{-1}}{2}, \frac{\phi^2}{2\sqrt{3}}, 0, \frac{1}{\sqrt{3}}, 0 \right),$$

$$\mathbf{q}_{g_g}^{D_{3d}} = q_{g_g} \left(\frac{1}{\sqrt{6}}, 0, -\sqrt{\frac{5}{6}}, 0 \right), \quad (12)$$

respectively³². Substituting these symmetrized deformations, Eqs. (11) and (12), into potential terms of model Hamiltonian (kinetic energy term is ignored), and then diagonalizing model Hamiltonian, we obtain the lowest adiabatic potential energies as

$$U^{D_{5d}} = \frac{1}{2} \omega_h^2 q_h^2 + V_{1h} q_h,$$

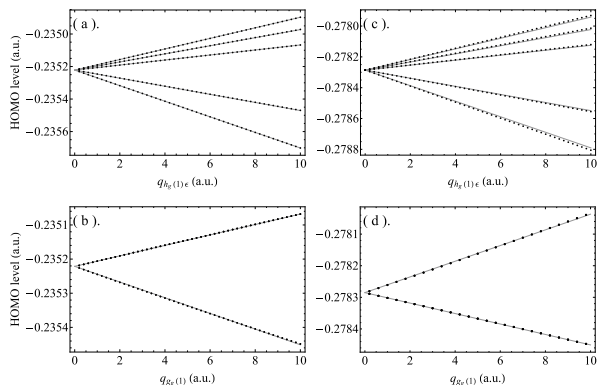


FIG. 1. The JT splitting of the HOMO levels with respect to $q_{h_g(1)\epsilon}$ ((a) and (c)) and $q_{g_g(1)a}$ ((b) and (d)) deformations (in atomic unit). (a) and (b) are calculated with B3LYP functional, while (c) and (d) are with CAM-B3LYP functional. The black points and gray lines indicate the DFT values and model energy, respectively.

$$U^{D_{3d}} = \frac{1}{2}\omega_g^2 q_g^2 + \frac{1}{2}\omega_h^2 q_h^2 + \frac{1}{3} \left(2V_g q_g + \sqrt{5}V_h q_h \right) \quad (13)$$

for D_{5d} and D_{3d} deformations, respectively. Furthermore, these global minima energies could be expressed in terms of stabilization energies (Eq. (5)), as¹⁴

$$\begin{aligned} E_{\text{JT}}^{D_{5d}} &= -E_{1h}^{\text{JT}}, \\ E_{\text{JT}}^{D_{3d}} &= -\frac{1}{9} (4E_g^{\text{JT}} + 5E_{2h}^{\text{JT}}). \end{aligned} \quad (14)$$

JT stabilization energies of C_{60}^+ are obtained using these equations and the calculated vibronic coupling parameters. When treating C_{60}^+ , we have to sum up contributions from all g_g and h_g modes. Manini *et al.* also have derived vibronic coupling parameters and JT stabilization energies in the same way with LDA.²³ Besides, there is always the stabilization due to the totally symmetric modes (Eq. (6)).

JT stabilization energies of C_{60}^+ have been calculated with different methods with various functionals. These methodologies to derive JT energies are classified into four. We denote the present method (I). In the second method, JT stabilization energy is directly obtained from the energy difference between high- and low-symmetric structures. This method was employed by Lykhin *et al.*⁷ with B3LYP. The third and the fourth methods, (III) and (IV), are called interaction mode approach^{37,38} and intrinsic distortion path approach³⁹⁻⁴², respectively. In both methods, vibronic coupling parameters or JT energies are extracted from optimized geometry with each subgroup of I_h . The interaction mode induces deformation along JT minima from high-symmetric coordinates and is expressed by a linear combination of normal modes of high-symmetric C_{60} . The coefficients of the linear combinations contain the information of the vibronic coupling. By expanding the difference of JT deformed and high-symmetry geometries, $\Delta\mathbf{R}_{\text{JT}}$, with the eigen modes

of mass-weighted normal modes \mathbf{e}_i ³¹ at high-symmetry structure as

$$\frac{V_i}{\omega_i^2} = c_i \sqrt{M} \Delta\mathbf{R}_{\text{JT}} \cdot \mathbf{e}_i, \quad (15)$$

the vibronic coupling parameters V_i could be obtained. The frequencies ω_i are obtained from first principles calculations and M is mass of carbon, and the coefficients c_i depend on the structure of the JT interaction matrix. This approach was used in Refs.^{25,43}. On the other hand, within the intrinsic distortion path analysis, the high-symmetric structure is expressed by the linear combination of the eigen vectors from low-symmetric structure. Combining the vibronic coupling parameters derived from the deformation, V_i' , and the frequencies at the low-symmetric structure, ω_i' , the JT energy could be written as $E_{\text{JT}} = \sum_i V_i'^2 / (2\omega_i'^2)$. The last method was applied to C_{60}^+ in Ref.²⁵.

JT stabilization energies in this work, as well as those from previous studies, are shown in Table II, from which we could see that CAM-B3LYP could enhance JT stabilization energies for D_{5d} and D_{3d} minima by 17% and 30% respectively compared to that with B3LYP. And JT stabilization energies obtained with both B3LYP and CAM-B3LYP are larger than those from LDA or PBE-related functionals. In particular, data calculated with LDA from Manini *et al.*,²³ is only about 60 % of the present data. The underestimation of JT energy by LDA method is consistent with the situation in C_{60}^- ²⁶. However, since with LDA methods (II) and (III) give similar data as the one by method (I),²³ the difference of these methods would not be the origin of discrepancies seen in B3LYP data. Thus, a possible reason is that the deformed geometry with B3LYP functional in Ref.²⁵ is the one at a local minima. For B3LYP, Ref.⁷ and present work give much close results, whereas the former is larger than the latter by 11 meV. So such a difference is expected to come from that JT stabilization energies contributed by totally symmetric modes, Eq. (6), are included in Ref.⁷. However, JT stabilization energy contributed from a_g modes in this work is about 3.5 meV (Table I), which is still smaller than 11 meV. The underestimation of vibronic coupling of totally symmetric modes may come from the lack of contributions from occupied orbitals and change of frequencies. In general, only the partially filled frontier orbitals contribute to the vibronic coupling to the JT modes due to the symmetry⁴⁴, whereas all occupied orbitals do contribute to vibronic coupling to the totally symmetric modes⁴⁵. Indeed, in the case of a planar molecule, picene, orbital vibronic coupling parameters for totally symmetric modes differ by 10-20 % from those obtained by fitting the gradients of total system energy⁴⁶. Frequencies can be changed due to the removal of electron by 5-15 %⁴⁷. Another possible origin of this discrepancy is non-linear vibronic coupling, however, such coupling is much weaker than linear vibronic coupling as in the case of C_{60} anions³².

TABLE II. Jahn-Teller energies of C_{60}^+ (meV) for D_{5d} and D_{3d} minima of the APES, respectively.

Functional	Method	D_{5d}	D_{3d}	Ref
B3LYP	(I)	110	30	Present
CAM-B3LYP	(I)	129	39	Present
LDA	(I)	69	22	²³
B3LYP	(II)	121	-	⁷
LDA	(III)	74	27	²⁵
OPBE	(III)	74	28	²⁵
B3LYP	(III)	80	32	²⁵
PBE	(III)	74	28	⁴³
LDA	(IV)	72	20	²⁵
OPBE	(IV)	74	21	²⁵
B3LYP	(IV)	94	25	²⁵

Besides these works, we note that Kern *et al.*¹³ have optimized the structure to simulate infrared (IR) absorption spectrum with BP86 functional, but JT energy was not derived.

IV. DISCUSSION

To fully reveal the molecular nature of C_{60}^+ , non-adiabatic dynamical Jahn-Teller effect is crucial. The most straightforward way would be exact diagonalizing the molecular Hamiltonian, which fully quantizes both nuclear and electronic coordinates, nevertheless, it is not practical. To partly overcome this difficulty, combining Jahn-Teller model Hamiltonian (3) with accurate enough vibronic coupling parameters is indispensable to derive low-energy states.

Vibronic coupling parameters of C_{60}^+ have been derived by using DFT calculations with LDA^{23,25} and B3LYP²⁴ functionals. As discussed in Sec. II, model Hamiltonian is described by one vibronic coupling parameter for each a_g and g_g mode, and two parameters for each h_g mode. Both parameters for the h_g modes, V_{1h} and V_{2h} , have been derived only in Ref.²³ and Ref.²⁵, while they have not in Ref.²⁴. Ramanantoanina *et al.*²⁵ shows that the magnitudes of derived coupling parameters obtained from the gradient of HOMO levels²³ and those from adiabatic potential energy surface agree well with each other, which has been also seen in C_{60}^- ^{26,32,33}. Thus, the present orbital vibronic coupling parameters derived from C_{60} must be close to the parameters for C_{60}^+ derived based on the definition.

The accuracy of LDA data have been discussed^{25,48} based on the comparison between experimental photoelectron spectra (PES)¹² and those from numerical simulation¹⁷. Indeed, PES is very useful to establish vibronic coupling parameters, whereas the simulation of PES requires high accuracy both in theoretical simulation and experiments. In the case of C_{60}^- , vibronic

coupling parameters derived from broad PES at high-temperature⁴⁹ have been proved to be overestimated by the simulation of high-resolution PES spectra²⁶. Furthermore, it was also found that the error bar of vibronic coupling parameters derived from broad PES is very large²⁶. Thus, the derivation of accurate coupling parameters is only possible if we have high-resolution PES spectra measured at low-temperature^{50,51}. In the case of C_{60}^+ , as pointed out by Manini *et al.*¹⁷, experimental PES is broad and fine structure of low-energy region due to vibronic coupling is completely smeared out, which prevents the direct comparison between theory and experiment. Moreover, in the case of PES of C_{60}^+ , theoretical ratio of the second strongest peak to the strongest one is smaller than those of experimental data, implying the underestimation of vibronic coupling by LDA. From this point, the present data larger than the LDA data by 40 % would give better agreement.

The quality of B3LYP calculations has been checked in C_{60} anions by comparing theoretical and experimental data in previous studies. Besides the good agreement between coupling parameters from B3LYP calculations and high-resolution PES²⁶, the good quality of B3LYP calculations also has been confirmed from Néel temperature⁵², spin gap⁵³, and the explanation for the origin of temperature evolution of infrared spectra⁴⁷ in Mott-insulating Cs_3C_{60} using the same vibronic coupling parameters. Furthermore, vibronic coupling parameters from B3LYP calculations tend to give good description of inelastic electron tunneling spectra of other organic molecule⁵⁴. All these facts show that B3LYP values are closer to the reality in C_{60}^+ , but there still a mismatch when compared with experimental data. The application of CAM-B3LYP could eliminate such mismatch of vibronic parameters in fullerene system, as shown in recent study of C_{60}^- ²⁸.

Although the derivation of vibronic coupling parameters is the first step toward full description of the molecular states of C_{60}^+ , we believe this is a crucial step. Once calculations of accurate enough vibronic states become possible, it is possible to interpret various spectra such as scanning tunneling measurements of C_{60} ⁵⁵, inverse PES⁵⁶ and angle resolved PES⁵⁷ to mention a few. Furthermore, present coupling parameters are derived based on the well-defined phase factor of normal modes which has been also used for orbital coupling parameters of LUMO³² and next LUMO²⁸. Therefore, by combining present coupling parameters with them, it is also possible to address complex vibronic problems of excited C_{60} ⁵⁸, and also to analyze *e.g.* luminescence spectra⁵⁹ and relaxation process and thermally activated delayed luminescence⁶⁰.

V. CONCLUSIONS

In this work, orbital vibronic coupling parameters for h_u HOMO level of C_{60} are derived using both B3LYP and

CAM-B3LYP hybrid functional. We believe that these vibronic coupling parameters are high accurate and close to the real situation. With these obtained coupling parameters, JT stabilization energies of C_{60}^+ are calculated, and JT structure at the minima of APES is confirmed to be D_{5d} , with the stabilization energy 110 meV and 129 meV calculated with B3LYP and CAM-B3LYP, respectively. JT stabilization energies in C_{60}^+ are about two times larger than that in C_{60}^- , suggesting the crucial role of the dynamical JT effect to reveal the actual situation of C_{60}^+ .

Present coupling parameters have been derived within the same framework used for our studies on ground and excited C_{60}^- . Thus, combining present data with that from other works, it is also possible to analyze the vibronic problems of excited C_{60} .

ACKNOWLEDGMENTS

The authors thank Dr. Naoya Iwahara and Prof. Dr. Liviu Chibotaru for fruitful discussions. They also gratefully acknowledge funding by the China Scholarship Council (CSC). Dr. Dan. Liu is supported by "the Fundamental Research Funds for the Central Universities" (G2019KY0517, G2019KY05104)

CONFLICT OF INTEREST

There are no conflicts to declare.

VI. APPENDIX

A. Clebsch-Gordan coefficients: $\hat{C}_{\Gamma\gamma}$

For the derivation of the vibronic Hamiltonian, the Clebsch-Gordan coefficients, $\hat{C}_{\Gamma\gamma}$ are taken from Ref.³², and listed below, in which $\phi = (1 + \sqrt{5})/2$, $\Gamma = g, 1h, 2h$, and $\gamma = a, x, y, z, \theta, \epsilon, \xi, \eta, \zeta$.

$$\hat{C}_{ga} = \begin{pmatrix} \frac{1}{2}\sqrt{\frac{3}{2}} & 0 & 0 & 0 & 0 \\ 0 & \frac{1}{2}\sqrt{\frac{3}{2}} & 0 & 0 & 0 \\ 0 & 0 & -\frac{1}{\sqrt{6}} & 0 & 0 \\ 0 & 0 & 0 & -\frac{1}{\sqrt{6}} & 0 \\ 0 & 0 & 0 & 0 & -\frac{1}{\sqrt{6}} \end{pmatrix} \quad (16)$$

$$\hat{C}_{gx} = \begin{pmatrix} 0 & 0 & -\frac{\phi}{4}\sqrt{\frac{5}{2}} & 0 & 0 \\ 0 & 0 & \frac{\phi^{-2}}{4}\sqrt{\frac{5}{6}} & 0 & 0 \\ -\frac{\phi}{4}\sqrt{\frac{5}{2}} & \frac{\phi^{-2}}{4}\sqrt{\frac{5}{6}} & 0 & 0 & 0 \\ 0 & 0 & 0 & 0 & \frac{1}{2}\sqrt{\frac{5}{6}} \\ 0 & 0 & 0 & \frac{1}{2}\sqrt{\frac{5}{6}} & 0 \end{pmatrix} \quad (17)$$

$$\hat{C}_{gy} = \begin{pmatrix} 0 & 0 & 0 & \frac{\phi^{-1}}{4}\sqrt{\frac{5}{2}} & 0 \\ 0 & 0 & 0 & -\frac{\phi^2}{4}\sqrt{\frac{5}{6}} & 0 \\ 0 & 0 & 0 & 0 & \frac{1}{2}\sqrt{\frac{5}{6}} \\ \frac{\phi^{-1}}{4}\sqrt{\frac{5}{2}} & -\frac{\phi^2}{4}\sqrt{\frac{5}{6}} & 0 & 0 & 0 \\ 0 & 0 & \frac{1}{2}\sqrt{\frac{5}{6}} & 0 & 0 \end{pmatrix} \quad (18)$$

$$\hat{C}_{gz} = \begin{pmatrix} 0 & 0 & 0 & 0 & \frac{1}{4}\sqrt{\frac{5}{2}} \\ 0 & 0 & 0 & 0 & \frac{5}{4\sqrt{6}} \\ 0 & 0 & 0 & \frac{1}{2}\sqrt{\frac{5}{6}} & 0 \\ 0 & 0 & \frac{1}{2}\sqrt{\frac{5}{6}} & 0 & 0 \\ \frac{1}{4}\sqrt{\frac{5}{2}} & \frac{5}{4\sqrt{6}} & 0 & 0 & 0 \end{pmatrix} \quad (19)$$

$$\hat{C}_{1h\theta} = \begin{pmatrix} \frac{\sqrt{5}}{16} & \frac{3\sqrt{3}}{16} & 0 & 0 & 0 \\ \frac{3\sqrt{3}}{16} & -\frac{\sqrt{5}}{16} & 0 & 0 & 0 \\ 0 & 0 & -\frac{\phi^{-2}}{4} & 0 & 0 \\ 0 & 0 & 0 & \frac{\phi^2}{4} & 0 \\ 0 & 0 & 0 & 0 & -\frac{\sqrt{5}}{4} \end{pmatrix} \quad (20)$$

$$\hat{C}_{1h\epsilon} = \begin{pmatrix} \frac{3\sqrt{3}}{16} & -\frac{\sqrt{5}}{16} & 0 & 0 & 0 \\ -\frac{\sqrt{5}}{16} & -\frac{3\sqrt{3}}{16} & 0 & 0 & 0 \\ 0 & 0 & -\frac{\sqrt{3}\phi}{4} & 0 & 0 \\ 0 & 0 & 0 & \frac{\sqrt{3}\phi^{-1}}{4} & 0 \\ 0 & 0 & 0 & 0 & \frac{\sqrt{3}}{4} \end{pmatrix} \quad (21)$$

$$\hat{C}_{1h\xi} = \begin{pmatrix} 0 & 0 & -\frac{\phi^{-2}}{4} & 0 & 0 \\ 0 & 0 & -\frac{\sqrt{3}\phi}{4} & 0 & 0 \\ -\frac{\phi^{-2}}{4} & -\frac{\sqrt{3}\phi}{4} & 0 & 0 & 0 \\ 0 & 0 & 0 & 0 & 0 \\ 0 & 0 & 0 & 0 & 0 \end{pmatrix} \quad (22)$$

$$\hat{C}_{1h\eta} = \begin{pmatrix} 0 & 0 & 0 & \frac{\phi^2}{4} & 0 \\ 0 & 0 & 0 & \frac{\sqrt{3}\phi^{-1}}{4} & 0 \\ 0 & 0 & 0 & 0 & 0 \\ \frac{\phi^2}{4} & \frac{\sqrt{3}\phi^{-1}}{4} & 0 & 0 & 0 \\ 0 & 0 & 0 & 0 & 0 \end{pmatrix} \quad (23)$$

$$\hat{C}_{1h\zeta} = \begin{pmatrix} 0 & 0 & 0 & 0 & -\frac{\sqrt{5}}{4} \\ 0 & 0 & 0 & 0 & \frac{\sqrt{3}}{4} \\ 0 & 0 & 0 & 0 & 0 \\ 0 & 0 & 0 & 0 & 0 \\ -\frac{\sqrt{5}}{4} & \frac{\sqrt{3}}{4} & 0 & 0 & 0 \end{pmatrix} \quad (24)$$

$$\hat{C}_{2h\theta} = \begin{pmatrix} \frac{9}{16} & -\frac{\sqrt{15}}{16} & 0 & 0 & 0 \\ -\frac{\sqrt{15}}{16} & -\frac{9}{16} & 0 & 0 & 0 \\ 0 & 0 & \frac{\phi}{4} & 0 & 0 \\ 0 & 0 & 0 & -\frac{\phi^{-1}}{4} & 0 \\ 0 & 0 & 0 & 0 & -\frac{1}{4} \end{pmatrix} \quad (25)$$

$$\hat{C}_{2h\epsilon} = \begin{pmatrix} -\frac{\sqrt{15}}{16} & -\frac{9}{16} & 0 & 0 & 0 \\ -\frac{9}{16} & \frac{\sqrt{15}}{16} & 0 & 0 & 0 \\ 0 & 0 & -\frac{\phi^{-2}}{4\sqrt{3}} & 0 & 0 \\ 0 & 0 & 0 & \frac{\phi^2}{4\sqrt{3}} & 0 \\ 0 & 0 & 0 & 0 & -\frac{1}{4}\sqrt{\frac{5}{3}} \end{pmatrix} \quad (26)$$

$$\hat{C}_{2h\xi} = \begin{pmatrix} 0 & 0 & \frac{\phi}{4} & 0 & 0 \\ 0 & 0 & -\frac{\phi^{-2}}{4\sqrt{3}} & 0 & 0 \\ \frac{\phi}{4} & -\frac{\phi^{-2}}{4\sqrt{3}} & 0 & 0 & 0 \\ 0 & 0 & 0 & 0 & \frac{1}{\sqrt{3}} \\ 0 & 0 & 0 & \frac{1}{\sqrt{3}} & 0 \end{pmatrix} \quad (27)$$

$$\hat{C}_{2h\eta} = \begin{pmatrix} 0 & 0 & 0 & -\frac{\phi^{-1}}{4\sqrt{3}} & 0 \\ 0 & 0 & 0 & \frac{\phi^2}{4\sqrt{3}} & 0 \\ 0 & 0 & 0 & 0 & \frac{1}{\sqrt{3}} \\ -\frac{\phi^{-1}}{4} & \frac{\phi^2}{4\sqrt{3}} & 0 & 0 & 0 \\ 0 & 0 & \frac{1}{\sqrt{3}} & 0 & 0 \end{pmatrix} \quad (28)$$

$$\hat{C}_{2h\zeta} = \begin{pmatrix} 0 & 0 & 0 & 0 & -\frac{1}{4} \\ 0 & 0 & 0 & 0 & -\frac{1}{4}\sqrt{\frac{5}{3}} \\ 0 & 0 & 0 & \frac{1}{\sqrt{3}} & 0 \\ 0 & 0 & \frac{1}{\sqrt{3}} & 0 & 0 \\ -\frac{1}{4} & -\frac{1}{4}\sqrt{\frac{5}{3}} & 0 & 0 & 0 \end{pmatrix} \quad (29)$$

¹E. K. Campbell, M. Holz, D. Gerlich, and J. P. Maier, "Laboratory confirmation of C_{60}^+ as the carrier of two diffuse interstellar bands," *Nature* **523**, 322 (2015).

²E. K. Campbell, M. Holz, J. P. Maier, D. Gerlich, G. A. H. Walker, and D. Bohlender, "Gas Phase Absorption Spectroscopy of C_{60}^+ and C_{70}^+ in a Cryogenic Ion Trap: Comparison with Astronomical Measurements," *The Astrophysical Journal* **822**, 17 (2016).

- ³S. Spieler, M. Kuhn, J. Postler, M. Simpson, R. Wester, P. Scheier, W. Ubachs, X. Bacalla, J. Bouwman, and H. Linnartz, " C_{60}^+ and the Diffuse Interstellar Bands: An Independent Laboratory Check," *The Astrophysical Journal* **846**, 168 (2017).
- ⁴K. M. Yamada, S. C. Ross, and F. Ito, " ^{13}C -substituted C_{60}^+ : Predictions of the rotational spectra," *Molecular Astrophysics* **6**, 9–15 (2017).
- ⁵D. V. Strelnikov, J. Jašík, D. Gerlich, M. Murata, Y. Murata, K. Komatsu, and J. Roithová, "Near- and Mid-IR Gas-Phase Absorption Spectra of $H_2@C_{60}^+-He$," *The Journal of Physical Chemistry A* **122**, 8162–8166 (2018).
- ⁶A. Kaiser, J. Postler, M. Onćák, M. Kuhn, M. Renzler, S. Spieler, M. Simpson, M. Gatchell, M. K. Beyer, R. Wester, F. A. Gianturco, P. Scheier, F. Calvo, and E. Yurtsever, "Isomeric Broadening of C_{60}^+ Electronic Excitation in Helium Droplets: Experiments Meet Theory," *The Journal of Physical Chemistry Letters* **9**, 1237–1242 (2018).
- ⁷A. O. Lykhin, S. Ahmadvand, and S. A. Varganov, "Electronic Transitions Responsible for C_{60}^+ Diffuse Interstellar Bands," *The Journal of Physical Chemistry Letters* **10**, 115–120 (2019).
- ⁸M. A. Cordiner, H. Linnartz, N. L. J. Cox, J. Cami, F. Najjarro, C. R. Proffitt, R. Lallement, P. Ehrenfreund, B. H. Foring, T. R. Gull, P. J. Sarre, and S. B. Charnley, "Confirming interstellar c_{60}^+ using the hubble space telescope," *The Astrophysical Journal* **875**, L28 (2019).
- ⁹C. C. Chancey and M. C. M. O'Brien, *The Jahn-Teller Effect in C_{60} and Other Icosahedral Complexes* (Princeton University Press, Princeton, 1997).
- ¹⁰I. B. Bersuker, *The Jahn-Teller Effect* (Cambridge University Press, Cambridge, 2006).
- ¹¹P. A. Brühwiler, A. J. Maxwell, P. Baltzer, S. Andersson, D. Arvanitis, L. Karlsson, and N. Mårtensson, "Vibronic coupling in the photoemission bands of condensed C_{60} ," *Chemical Physics Letters* **279**, 85–91 (1997).
- ¹²S. E. Canton, A. J. Yench, E. Kukuk, J. D. Bozek, M. C. A. Lopes, G. Snell, and N. Berrah, "Experimental Evidence of a Dynamic Jahn-Teller Effect in C_{60}^+ ," *Phys. Rev. Lett.* **89**, 045502 (2002).
- ¹³B. Kern, D. Strelnikov, P. Weis, A. Böttcher, and M. M. Kappes, "IR Absorptions of C_{60}^+ and C_{60}^- in Neon Matrixes," *J. Phys. Chem. A* **117**, 8251 (2013).
- ¹⁴A. Ceulemans and P. W. Fowler, "The Jahn-Teller instability of fivefold degenerate states in icosahedral molecules," *The Journal of Chemical Physics* **93**, 1221–1234 (1990).
- ¹⁵C. P. Moate, M. C. M. O'Brien, J. L. Dunn, C. A. Bates, Y. M. Liu, and V. Z. Polinger, " $H \otimes h$: A Jahn-Teller Coupling That Really Does Reduce the Degeneracy of the Ground State," *Phys. Rev. Lett.* **77**, 4362–4365 (1996).
- ¹⁶P. De Los Rios, N. Manini, and E. Tosatti, "Dynamical Jahn-Teller effect and Berry phase in positively charged fullerenes: Basic considerations," *Phys. Rev. B* **54**, 7157–7167 (1996).
- ¹⁷N. Manini, P. Gattari, and E. Tosatti, "Jahn-Teller Spectral Fingerprint in Molecular Photoemission: C_{60} ," *Phys. Rev. Lett.* **91**, 196402 (2003).
- ¹⁸E. Lijnen and A. Ceulemans, "Berry phase and entanglement in the icosahedral $H \otimes (g \oplus 2h)$ Jahn-Teller system with trigonal minima," *Phys. Rev. B* **71**, 014305 (2005).
- ¹⁹I. D. Hands, L. M. Sindi, J. L. Dunn, and C. A. Bates, "Theoretical treatment of pseudorotation in the Jahn-Teller C_{60}^+ ion," *Phys. Rev. B* **74**, 115410 (2006).
- ²⁰I. D. Hands, J. L. Dunn, W. A. Diery, and C. A. Bates, "Vibronic coupling in the icosahedral C_{60}^{2+} Jahn-Teller cation: Repercussions of the nonsimple reducibility of the $H \otimes H$ product," *Phys. Rev. B* **73**, 115435 (2006).
- ²¹I. D. Hands, W. A. Diery, C. A. Bates, and J. L. Dunn, "Jahn-teller effects in the C_{60}^{2+} cation undergoing D_{2h} distortion," *Phys. Rev. B* **76**, 085426 (2007).
- ²²A. Ceulemans, E. Lijnen, P. W. Fowler, R. B. Mallion, and T. Pisanski, "S5 graphs as model systems for icosahedral jahn-teller problems,"

- Theoretical Chemistry Accounts **131** (2012), 10.1007/s00214-012-1246-31.
- ²³N. Manini, A. D. Corso, M. Fabrizio, and E. Tosatti, "Electron-vibration coupling constants in positively charged fullerene," *Philosophical Magazine B* **81**, 793–812 (2001).
- ²⁴M. Saito, "Electron-phonon coupling of electron- or hole-injected C₆₀," *Phys. Rev. B* **65**, 220508 (2002).
- ²⁵H. Ramanantoanina, M. Zlatar, P. García-Fernández, C. Daul, and M. Gruden-Pavlović, "General treatment of the multimode jahn-teller effect: study of fullerene cations," *Phys. Chem. Chem. Phys.* **15**, 1252–1259 (2013).
- ²⁶N. Iwahara, T. Sato, K. Tanaka, and L. F. Chibotaru, "Vibronic coupling in C₆₀⁻ anion revisited: Derivations from photoelectron spectra and DFT calculations," *Phys. Rev. B* **82**, 245409 (2010).
- ²⁷C. Faber, J. L. Janssen, M. Côté, E. Runge, and X. Blase, "Electron-phonon coupling in the C₆₀ fullerene within the many-body *GW* approach," *Phys. Rev. B* **84**, 155104 (2011).
- ²⁸Z. Huang and D. Liu, "Dynamical jahn-teller effect in the first excited c₆₀⁻," *International Journal of Quantum Chemistry* **120**, e26148 (2020).
- ²⁹H. W. Kroto, J. R. Heath, S. C. O'Brien, R. F. Curl, and R. E. Smalley, "C₆₀: Buckminsterfullerene," *Nature* **318**, 162–163 (1985).
- ³⁰H. A. Jahn and E. Teller, "Stability of Polyatomic Molecules in Degenerate Electronic States. I. Orbital Degeneracy," *Proc. R. Soc. Lond. A* **161**, 220 (1937).
- ³¹T. Inui, Y. Tanabe, and Y. Onodera, *Group Theory and Its Applications in Physics* (Springer-Verlag, Berlin and Heidelberg, 1990).
- ³²D. Liu, Y. Niwa, N. Iwahara, T. Sato, and L. F. Chibotaru, "Quadratic Jahn-Teller effect of fullerene anions," *Phys. Rev. B* **98**, 035402 (2018).
- ³³J. Laflamme Janssen, M. Côté, S. G. Louie, and M. L. Cohen, "Electron-phonon coupling in C₆₀ using hybrid functionals," *Phys. Rev. B* **81**, 073106 (2010).
- ³⁴A. L. Fetter and D. Walecka, *Quantum Theory of Many-Particle Systems* (Dover Publishing, Inc., New York, 2003).
- ³⁵M. J. Frisch, G. W. Trucks, H. B. Schlegel, G. E. Scuseria, M. A. Robb, J. R. Cheeseman, G. Scalmani, V. Barone, G. A. Petersson, H. Nakatsuji, X. Li, M. Caricato, A. V. Marenich, J. Bloino, B. G. Janesko, R. Gomperts, B. Mennucci, H. P. Hratchian, J. V. Ortiz, A. F. Izmaylov, J. L. Sonnenberg, D. Williams-Young, F. Ding, F. Lipparini, F. Egidi, J. Goings, B. Peng, A. Petrone, T. Henderson, D. Ranasinghe, V. G. Zakrzewski, J. Gao, N. Rega, G. Zheng, M. Liang, M. Hada, M. Ehara, K. Toyota, R. Fukuda, J. Hasegawa, M. Ishida, T. Nakajima, Y. Honda, O. Kitao, H. Nakai, T. Vreven, K. Throssell, J. A. Montgomery, Jr., J. E. Peralta, F. Ogliaro, M. J. Bearpark, J. J. Heyd, E. N. Brothers, K. N. Kudin, V. N. Staroverov, T. A. Keith, R. Kobayashi, J. Normand, K. Raghavachari, A. P. Rendell, J. C. Burant, S. S. Iyengar, J. Tomasi, M. Cossi, J. M. Millam, M. Klene, C. Adamo, R. Cammi, J. W. Ochterski, R. L. Martin, K. Morokuma, O. Farkas, J. B. Foresman, and D. J. Fox, "Gaussian16 Revision C.01," (2016), gaussian Inc. Wallingford CT.
- ³⁶A. D. Liehr, "Topological aspects of the conformational stability problem. Part I. Degenerate electronic states," *J. Phys. Chem.* **67**, 389 (1963).
- ³⁷V. P. Khlopin, V. Z. Polinger, and I. B. Bersuker, "The jahn-teller effect in icosahedral molecules and complexes," *Theoretica chimica acta* **48**, 87–101 (1978).
- ³⁸I. B. Bersuker and V. Z. Polinger, *Vibronic Interactions in Molecules and Crystals* (Springer-Verlag, Berlin, 1989).
- ³⁹R. Bruyndonckx, C. Daul, P. T. Manoharan, and E. Deiss, "A nonempirical approach to ground-state jahn-teller distortion: Case study of vcl₄," *Inorganic Chemistry* **36**, 4251–4256 (1997).
- ⁴⁰M. Zlatar, C.-W. Schlöpfer, and C. Daul, "A new method to describe the multimode jahn-teller effect using density functional theory," in *The Jahn-Teller Effect* (Springer, 2009) pp. 131–165.
- ⁴¹M. Zlatar, M. Gruden-Pavlović, C.-W. Schlöpfer, and C. Daul, "Intrinsic distortion path in the analysis of the jahn-teller effect," *Journal of Molecular Structure: THEOCHEM* **954**, 86–93 (2010).
- ⁴²M. Zlatar and M. Gruden, "Calculation of the jahn-teller parameters with dft," 2019, 1 (2019).
- ⁴³J. T. Muya, H. Ramanantoanina, C. Daul, M. T. Nguyen, G. Gopakumar, and A. Ceulemans, "Jahn-Teller instability in cationic boron and carbon buckyballs B₈₀⁺ and C₆₀⁺: a comparative study," *Phys. Chem. Chem. Phys.* **15**, 2829–2835 (2013).
- ⁴⁴T. Sato, K. Tokunaga, and K. Tanaka, "Vibronic coupling in cyclopentadienyl radical: A method for calculation of vibronic coupling constant and vibronic coupling density analysis," *J. Chem. Phys.* **124**, 024314 (2006).
- ⁴⁵T. Sato, K. Tokunaga, and K. Tanaka, "Vibronic Coupling in Naphthalene Anion: Vibronic Coupling Density Analysis for Totally Symmetric Vibrational Modes," *J. Phys. Chem. A* **112**, 758 (2008).
- ⁴⁶T. Sato, N. Iwahara, and K. Tanaka, "Critical reinvestigation of vibronic couplings in picene from view of vibronic coupling density analysis," *Phys. Rev. B* **85**, 161102 (2012).
- ⁴⁷Y. Matsuda, N. Iwahara, K. Tanigaki, and L. F. Chibotaru, "Manifestation of vibronic dynamics in infrared spectra of mott insulating fullerenes," *Phys. Rev. B* **98**, 165410 (2018).
- ⁴⁸P. Ponzellini, *Computation of the paramagnetic g-factor for the fullerene monocation and monoanion*, Master's thesis, Milan University (2014).
- ⁴⁹O. Gunnarsson, H. Handschuh, P. S. Bechthold, B. Kessler, G. Ganteför, and W. Eberhardt, "Photoemission Spectra of C₆₀⁻: Electron-Phonon Coupling, Jahn-Teller Effect, and Superconductivity in the Fullerenes," *Phys. Rev. Lett.* **74**, 1875 (1995).
- ⁵⁰X.-B. Wang, H.-K. Woo, and L.-S. Wang, "Vibrational cooling in a cold ion trap: Vibrationally resolved photoelectron spectroscopy of cold C₆₀⁻ anions," *J. Chem. Phys.* **123**, 051106 (2005).
- ⁵¹D. L. Huang, P. D. Dau, H. T. Liu, and L. S. Wang, "High-resolution photoelectron imaging of cold C₆₀⁻ anions and accurate determination of the electron affinity of C₆₀," *J Chem Phys* **140**, 224315 (2014).
- ⁵²N. Iwahara and L. F. Chibotaru, "Dynamical Jahn-Teller Effect and Antiferromagnetism in Cs₃C₆₀," *Phys. Rev. Lett.* **111**, 056401 (2013).
- ⁵³D. Liu, N. Iwahara, and L. F. Chibotaru, "Dynamical jahn-teller effect of fullerene anions," *Phys. Rev. B* **97**, 115412 (2018).
- ⁵⁴K. Shizu, T. Sato, and K. Tanaka, "Inelastic electron tunneling spectra and vibronic coupling density analysis of 2,5-dimercapto-1,3,4-thiadiazole and tetrathiafulvalene dithiol," *Nanoscale* **2**, 2186–2194 (2010).
- ⁵⁵T. Frederiksen, K. J. Franke, A. Arnau, G. Schulze, J. I. Pascual, and N. Lorente, "Dynamic Jahn-Teller effect in electronic transport through single C₆₀ molecules," *Phys. Rev. B* **78**, 233401 (2008).
- ⁵⁶C. Große, P. Merino, A. Roslowska, O. Gunnarsson, K. Kuhnke, and K. Kern, "Submolecular Electroluminescence Mapping of Organic Semiconductors," *ACS Nano* **11**, 1230–1237 (2017).
- ⁵⁷D. W. Latzke, C. Ojeda-Aristizabal, J. D. Denlinger, R. Reno, A. Zettl, and A. Lanzara, "Orbital character effects in the photon energy and polarization dependence of pure c60 photoemission," *ACS Nano* **13**, 12710–12718 (2019).
- ⁵⁸Q. C. Qiu, L. F. Chibotaru, and A. Ceulemans, "Product jahn-teller systems: The {T₁ ⊕ H} ⊗ (g ⊕ 2h) icosahedral exciton," *Phys. Rev. B* **65**, 035104 (2001).
- ⁵⁹I. Akimoto and K.-i. Kan'no, "Photoluminescence and Near-Edge Optical Absorption in the Low-Temperature Phase of Pristine C₆₀ Single Crystals," *Journal of the Physical Society of Japan* **71**, 630–643 (2002).
- ⁶⁰A. G. Stepanov, M. T. Portella-Oberli, A. Sassara, and M. Chergui, "Ultrafast intramolecular relaxation of C₆₀," *Chemical Physics Letters* **358**, 516 – 522 (2002).

Supplement Material: First principles study of the vibronic coupling in positively charged C_{60}^+

Zhishuo Huang^{1,a)} and Dan Liu^{2,1,b)}

¹*Theory of Nanomaterials Group, KU Leuven, Celestijnenlaan 200F, B-3001 Leuven, Belgium*

²*Institute of Flexible Electronics (IFE), Northwestern Polytechnical University, 127 West Youyi Road, Xi'an, 710072, Shaanxi, China*

^{a)}Electronic address: zhishuohuang@gmail.com

^{b)}Electronic address: iamdliu@nwpu.edu.cn

Supplemental Materials contain the JT splitting of the HOMO levels with respect to $q_{h\epsilon}$ and q_{ga} deformations.

VII. JT SPLITTING OF THE HOMO LEVELS

There are eight $q_{h\epsilon}$ and six q_{ga} deformations, which are distinguished by the subindex, as $q_{h(1)\epsilon}$ corresponding to the first $q_{h\epsilon}$ deformation.

The DFT data with B3LYP hybrid functional and the definition of the phase factors of the normal modes are taken from Ref.³². The fitting for of the DFT HOMO levels to the model hamiltonian for $q_{h_g(i)\epsilon}$, $i = 2, 3, 4, 5, 6, 7, 8$ are shown in Fig. 2, 3, 4, 5, 6, 7 and 8, while $q_{g_g(i)}$, $i = 2, 3, 4, 5, 6$ are shown in Fig. 9, 10, 11, 12, and 13.

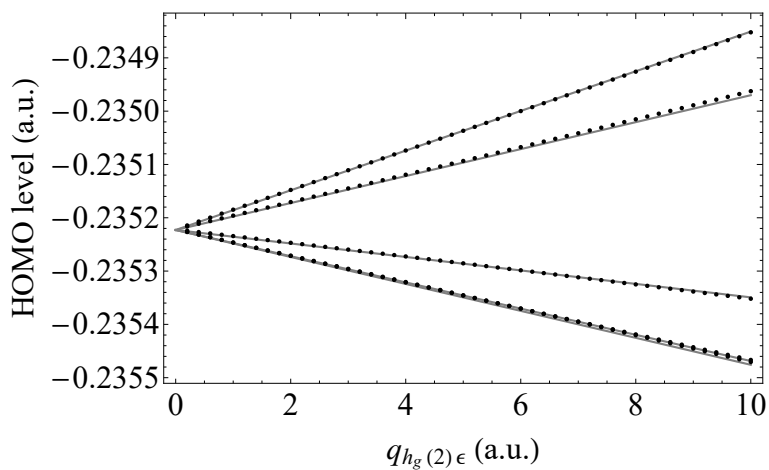


FIG. 2. The JT splitting of the HOMO levels calculated by B3LYP with respect to $q_{h_g(2)\epsilon}$ deformation (in atomic unit). The black points and gray lines indicate the DFT values and model energy, respectively.

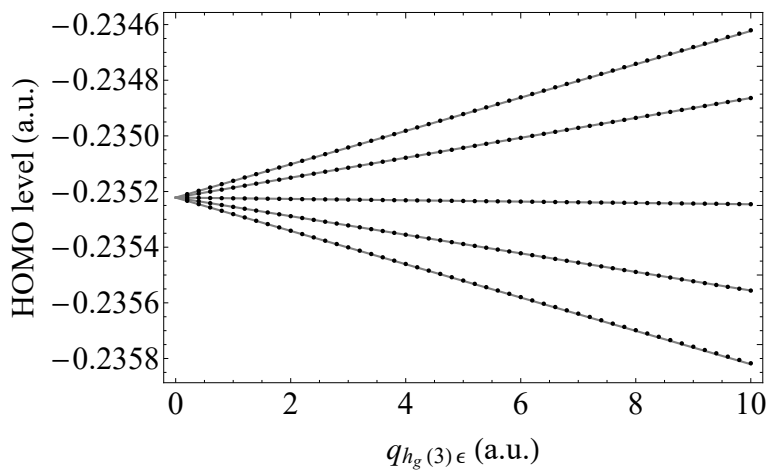


FIG. 3. The JT splitting of the HOMO levels calculated by B3LYP with respect to $q_{h_g(3)\epsilon}$ deformation (in atomic unit). The black points and gray lines indicate the DFT values and model energy, respectively.

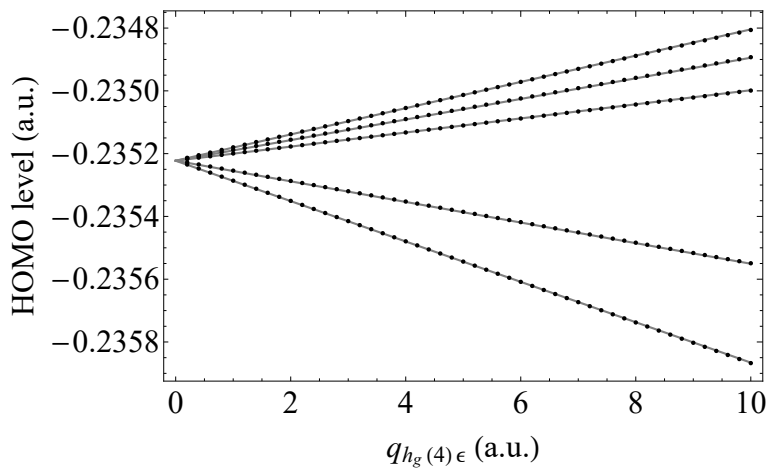


FIG. 4. The JT splitting of the HOMO levels calculated by B3LYP with respect to $q_{h_g(4)\epsilon}$ deformation (in atomic unit). The black points and gray lines indicate the DFT values and model energy, respectively.

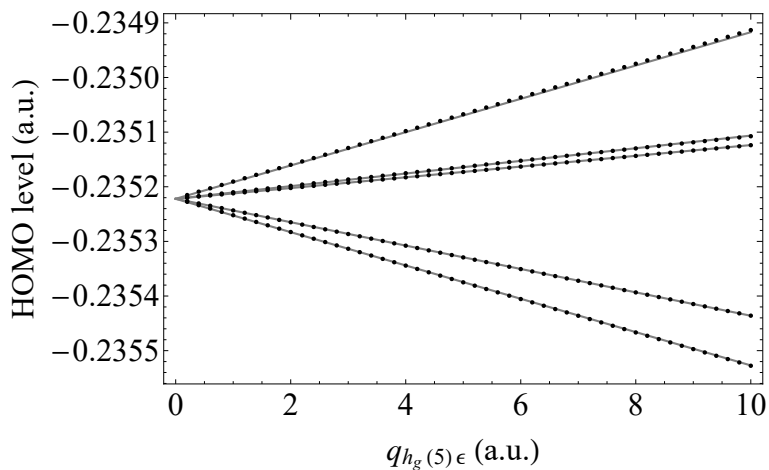


FIG. 5. The JT splitting of the HOMO levels calculated by B3LYP with respect to $q_{h_g(5)}\epsilon$ deformation (in atomic unit). The black points and gray lines indicate the DFT values and model energy, respectively.

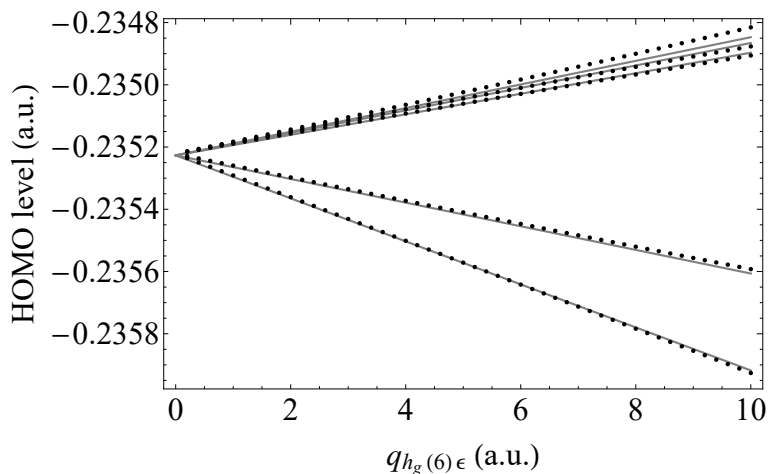


FIG. 6. The JT splitting of the HOMO levels calculated by B3LYP with respect to $q_{h_g(6)}\epsilon$ deformation (in atomic unit). The black points and gray lines indicate the DFT values and model energy, respectively.

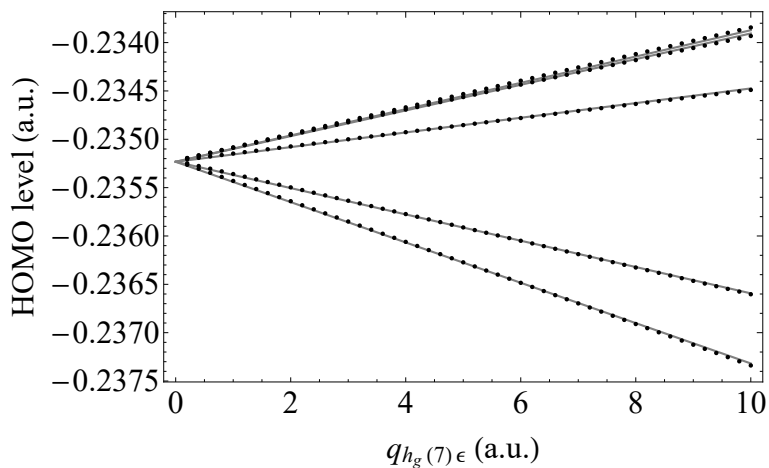


FIG. 7. The JT splitting of the HOMO levels calculated by B3LYP with respect to $q_{h_g(7)}\epsilon$ deformation (in atomic unit). The black points and gray lines indicate the DFT values and model energy, respectively.

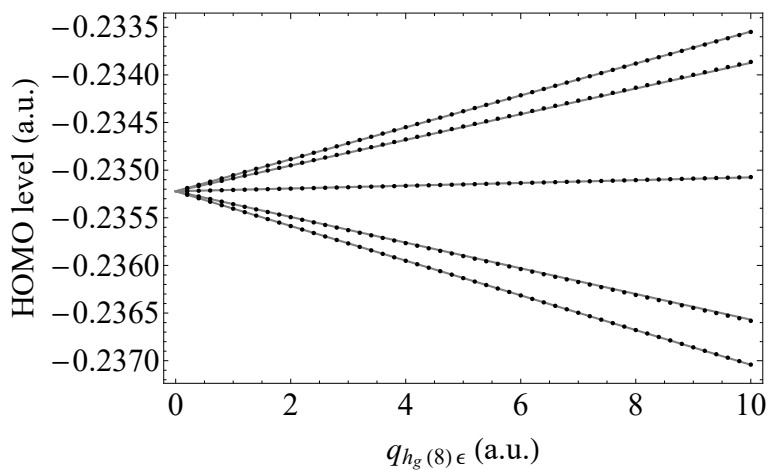


FIG. 8. The JT splitting of the HOMO levels calculated by B3LYP with respect to $q_{hg(8)}\epsilon$ deformation (in atomic unit). The black points and gray lines indicate the DFT values and model energy, respectively.

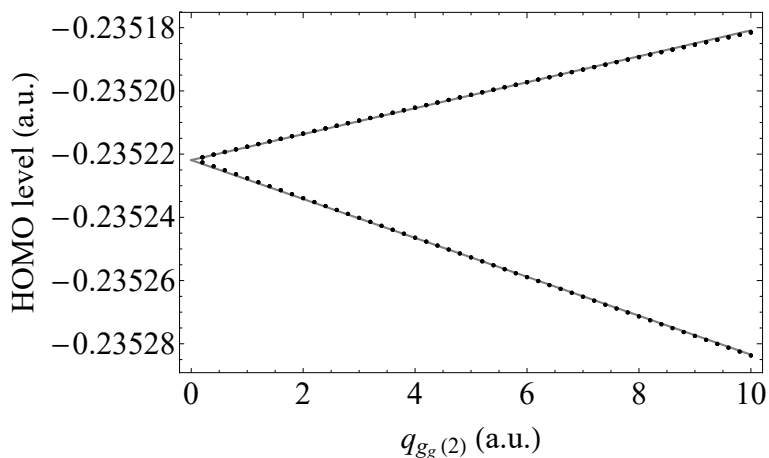


FIG. 9. The JT splitting of the HOMO levels calculated by B3LYP with respect to $q_{gg(2)}\epsilon$ deformation (in atomic unit). The black points and gray lines indicate the DFT values and model energy, respectively.

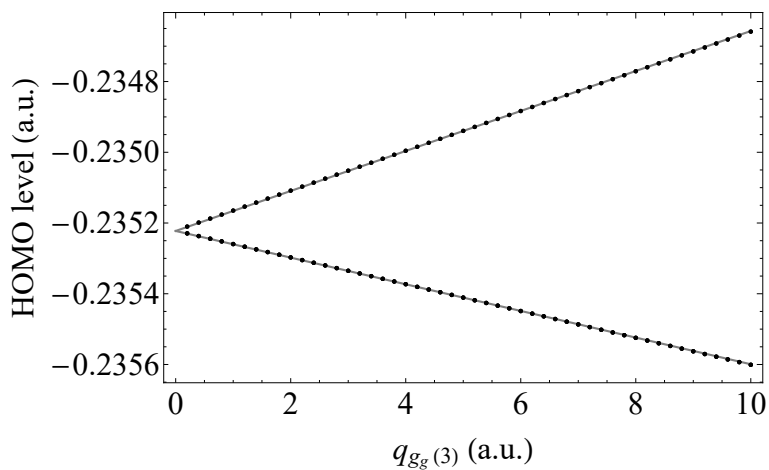


FIG. 10. The JT splitting of the HOMO levels calculated by B3LYP with respect to $q_{gg(3)}\epsilon$ deformation (in atomic unit). The black points and gray lines indicate the DFT values and model energy, respectively.

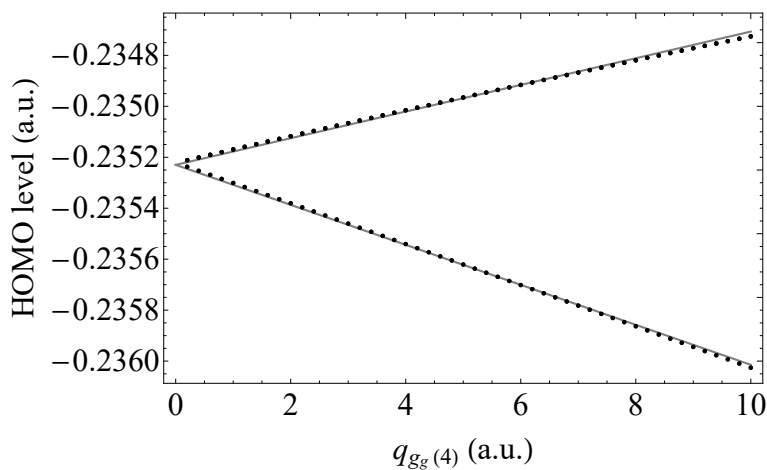


FIG. 11. The JT splitting of the HOMO levels calculated by B3LYP with respect to $q_{g_g(4)\epsilon}$ deformation (in atomic unit). The black points and gray lines indicate the DFT values and model energy, respectively.

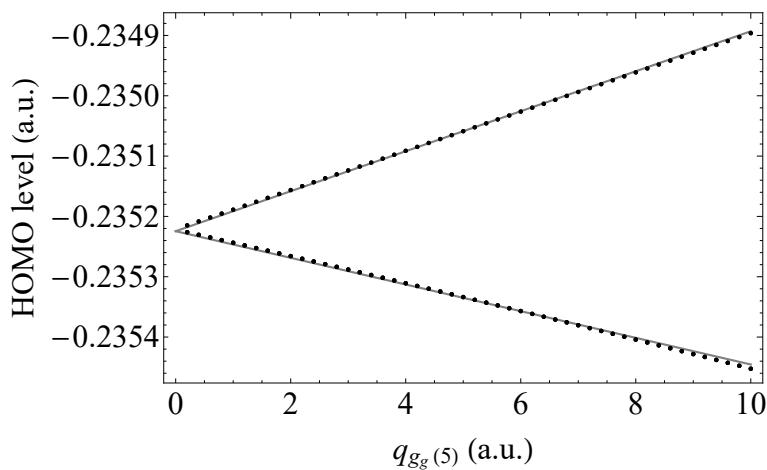


FIG. 12. The JT splitting of the HOMO levels calculated by B3LYP with respect to $q_{g_g(5)\epsilon}$ deformation (in atomic unit). The black points and gray lines indicate the DFT values and model energy, respectively.

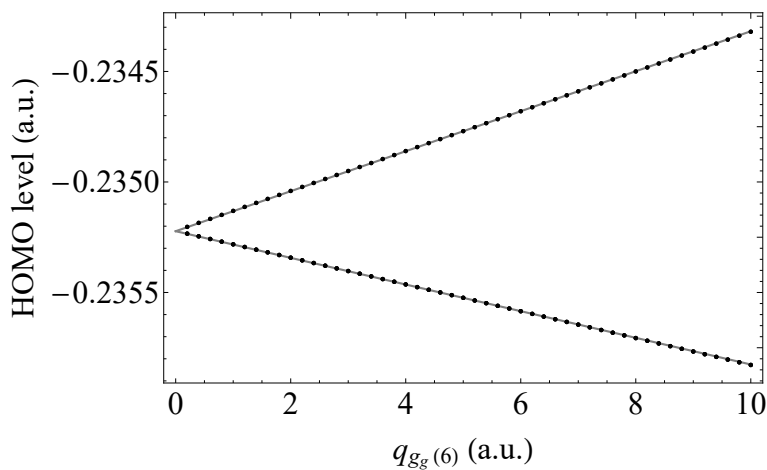


FIG. 13. The JT splitting of the HOMO levels calculated by B3LYP with respect to $q_{g_g(6)\epsilon}$ deformation (in atomic unit). The black points and gray lines indicate the DFT values and model energy, respectively.

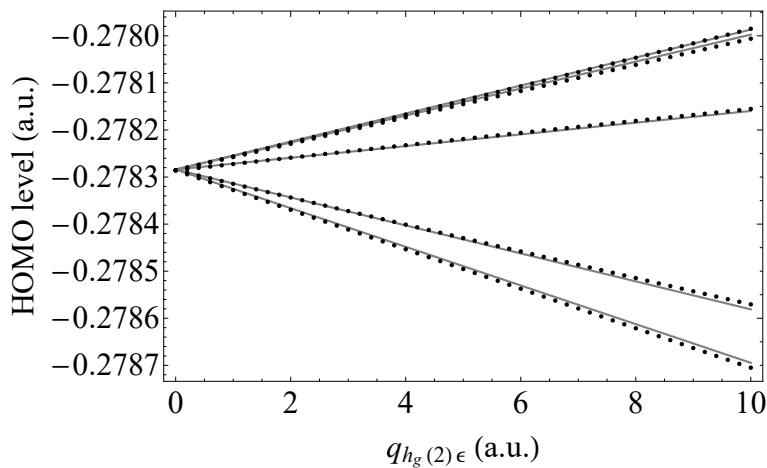


FIG. 14. The JT splitting of the HOMO levels calculated by CAM-B3LYP with respect to $q_{h_g(2)}\epsilon$ deformation (in atomic unit). The black points and gray lines indicate the DFT values and model energy, respectively.

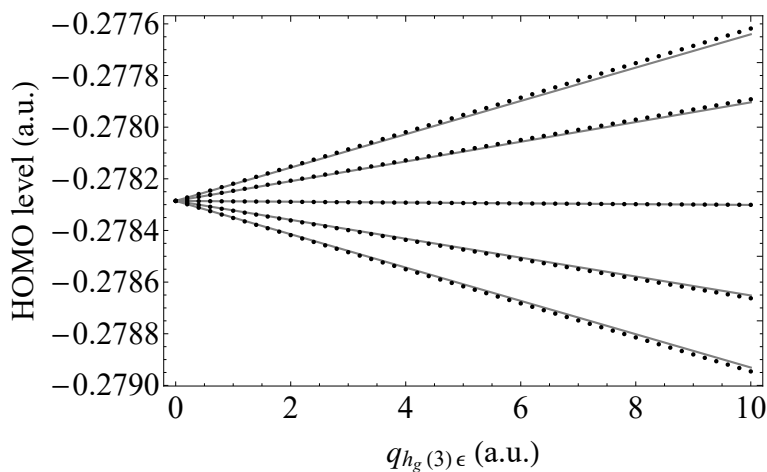


FIG. 15. The JT splitting of the HOMO levels calculated by CAM-B3LYP with respect to $q_{h_g(3)}\epsilon$ deformation (in atomic unit). The black points and gray lines indicate the DFT values and model energy, respectively.

Considering CAM-B3LYP functional, Fig. 14, 15, 16, 17, 18, 19 and 20 depict the fitting of $q_{h_g(i)}\epsilon$, $i = 2, 3, 4, 5, 6, 7, 8$, with Fig. 21, 22, 23, 24, and 25 for $q_{g_g(i)}$, $i = 2, 3, 4, 5, 6$.

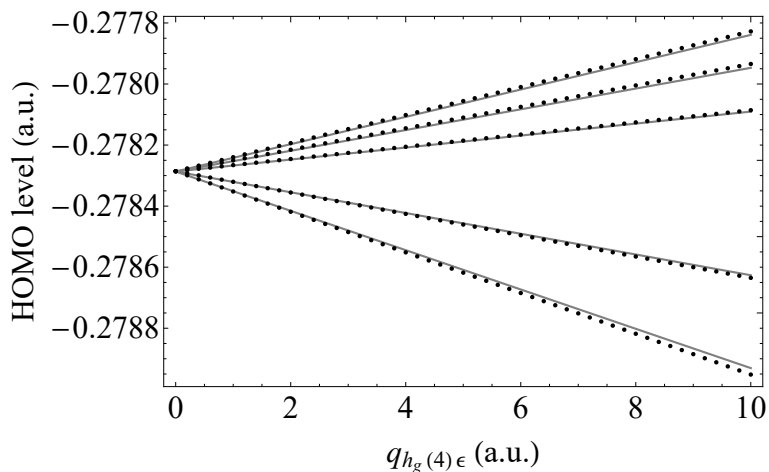


FIG. 16. The JT splitting of the HOMO levels calculated by CAM-B3LYP with respect to $q_{h_g(4)}\epsilon$ deformation (in atomic unit). The black points and gray lines indicate the DFT values and model energy, respectively.

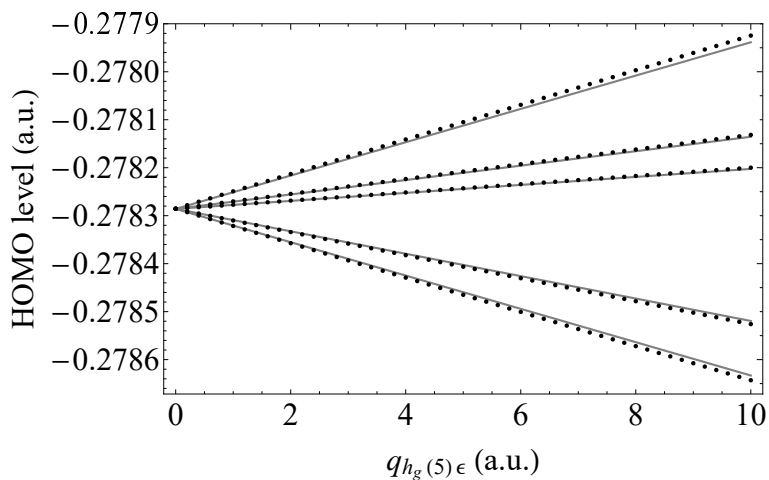


FIG. 17. The JT splitting of the HOMO levels calculated by CAM-B3LYP with respect to $q_{h_g(5)}\epsilon$ deformation (in atomic unit). The black points and gray lines indicate the DFT values and model energy, respectively.

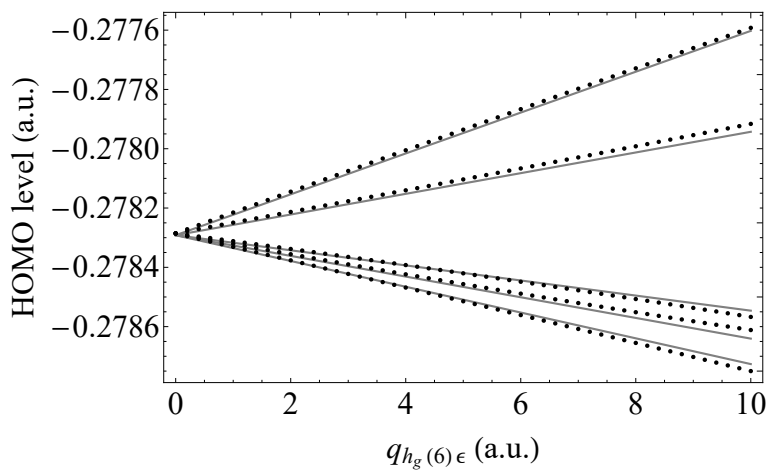


FIG. 18. The JT splitting of the HOMO levels calculated by CAM-B3LYP with respect to $q_{h_g(6)}\epsilon$ deformation (in atomic unit). The black points and gray lines indicate the DFT values and model energy, respectively.

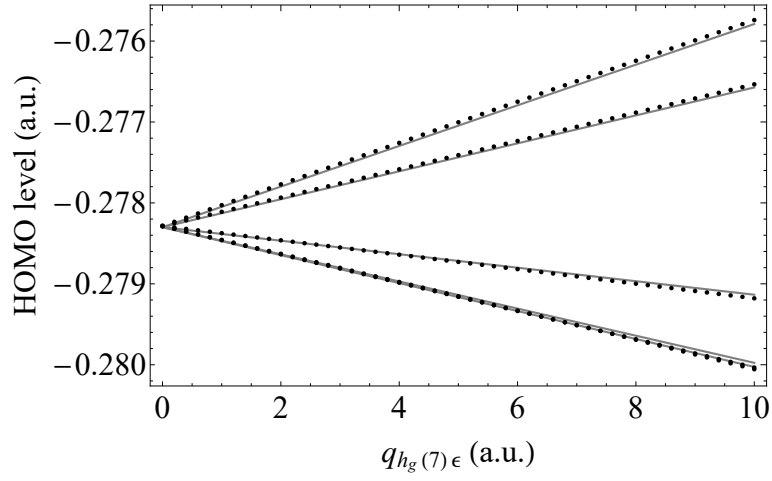


FIG. 19. The JT splitting of the HOMO levels calculated by CAM-B3LYP with respect to $q_{hg(7)\epsilon}$ deformation (in atomic unit). The black points and gray lines indicate the DFT values and model energy, respectively.

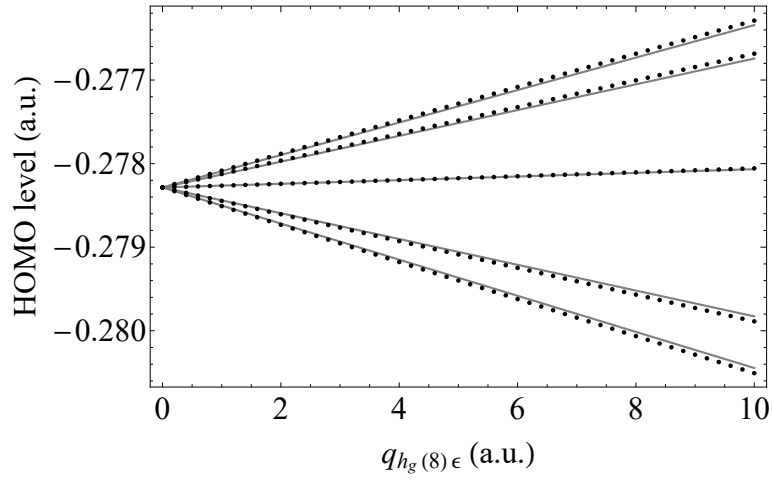


FIG. 20. The JT splitting of the HOMO levels calculated by CAM-B3LYP with respect to $q_{hg(8)\epsilon}$ deformation (in atomic unit). The black points and gray lines indicate the DFT values and model energy, respectively.

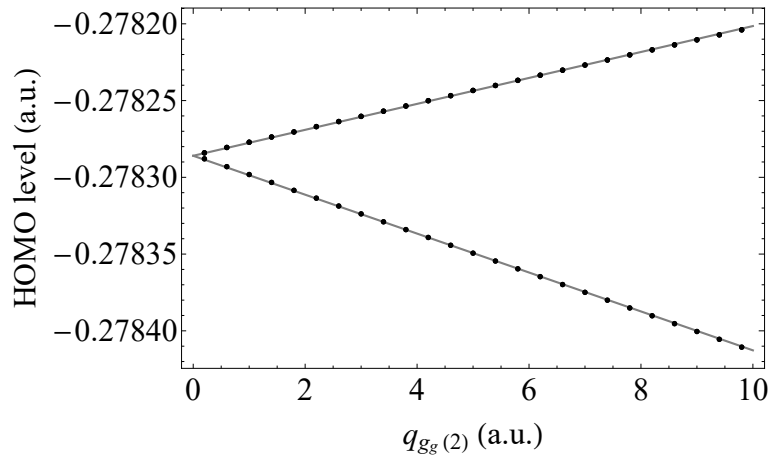


FIG. 21. The JT splitting of the HOMO levels calculated by CAM-B3LYP with respect to $q_{gg(2)\epsilon}$ deformation (in atomic unit). The black points and gray lines indicate the DFT values and model energy, respectively.

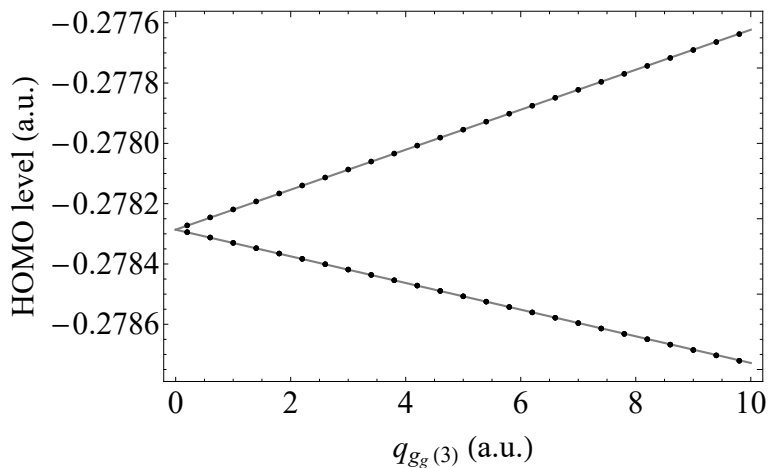


FIG. 22. The JT splitting of the HOMO levels calculated by CAM-B3LYP with respect to $q_{g_g(3)\epsilon}$ deformation (in atomic unit). The black points and gray lines indicate the DFT values and model energy, respectively.

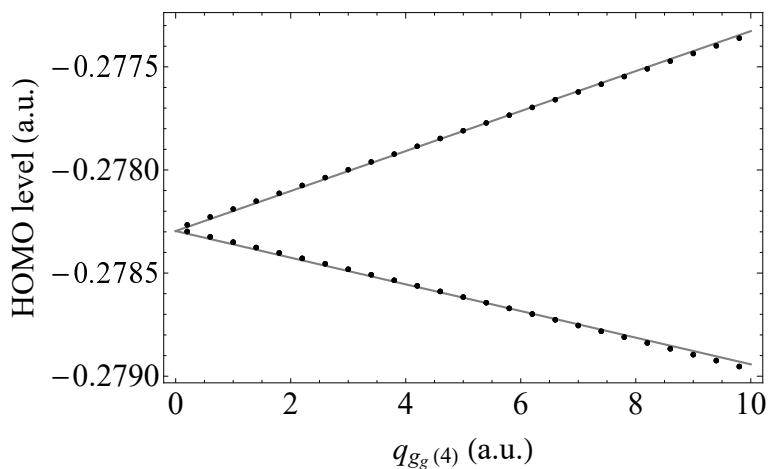


FIG. 23. The JT splitting of the HOMO levels calculated by CAM-B3LYP with respect to $q_{g_g(4)\epsilon}$ deformation (in atomic unit). The black points and gray lines indicate the DFT values and model energy, respectively.

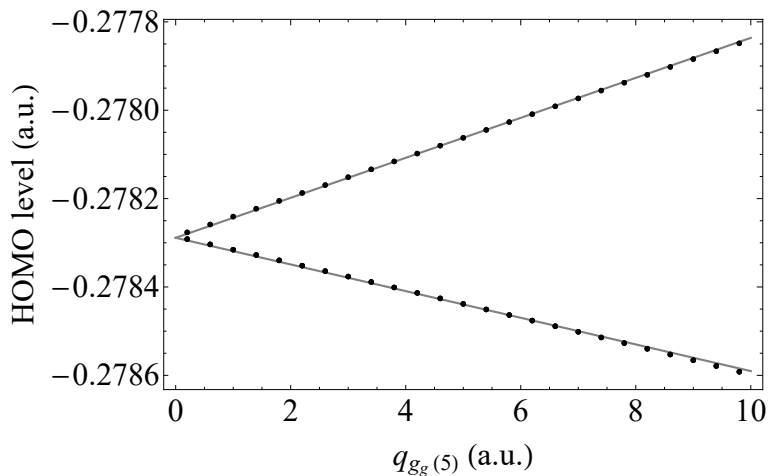


FIG. 24. The JT splitting of the HOMO levels calculated by CAM-B3LYP with respect to $q_{g_g(5)\epsilon}$ deformation (in atomic unit). The black points and gray lines indicate the DFT values and model energy, respectively.

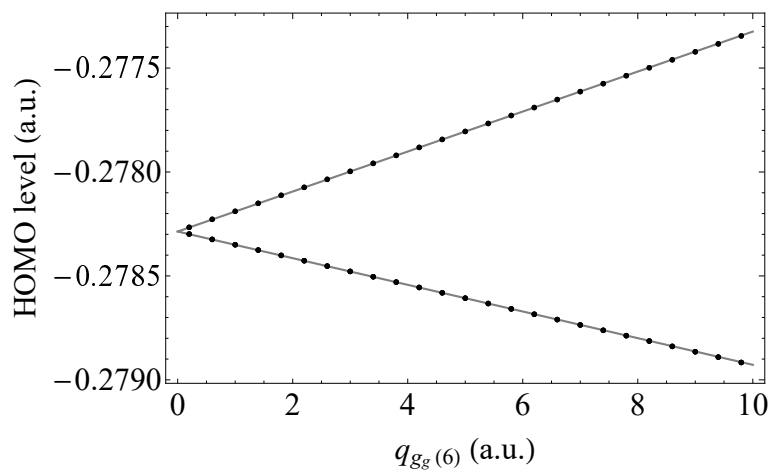


FIG. 25. The JT splitting of the HOMO levels calculated by CAM-B3LYP with respect to $q_{g_g(6)\epsilon}$ deformation (in atomic unit). The black points and gray lines indicate the DFT values and model energy, respectively.